Multi-colour hues of the Universe observed with AstroSat

K. P. Singh[1,*] and D. Bhattacharya[2]

[1]Department of Astronomy and Astrophysics, Tata Institute of Fundamental Research, Homi Bhabha Road, Mumbai 400 005, India
[2]Inter-University Centre for Astronomy and Astrophysics, Post Bag 4, Ganeshkhind, Pune 411 007, India

India's space astronomy observatory AstroSat was launched on 28 September 2015, carrying instruments to observe cosmic sources over a large spectral band, from optical/UV to hard X-rays. The mission, with all its payloads, has been operating successfully since its launch. After an initial period of performance verification and calibration, the satellite is now in full science operation. This article gives a brief introduction about the capabilities of the mission and presents some of the early science results.

Keywords: Active galaxies, cosmic sources, multi-wavelength astronomy, multi-colour hues, supernova remnants.

Introduction

ASTROSAT, India's first multiwavelength observatory, launched on 28 September 2015 from Sriharikota on the southeast coast of India by the C-30 Polar Satellite Launch Vehicle, carries a multitude of co-aligned optical, ultraviolet (UV) and X-ray telescopes and detectors to observe the universe. Its wide-band X-ray instruments with overlapping energy response, and simultaneous optical and UV observations of any cosmic object in the sky make it a unique mission to address a host of scientific issues in X-ray and UV astronomy. There are no other international observatories at present having this range of spectral coverage in one mission.

AstroSat, weighing about 1.5 tonnes, was launched into a circular orbit 650 km above the Earth with an inclination of ~6° and is expected to have a nominal lifetime of ~5 years. All operations – from tele-command and data reception via telemetry are carried out from ISTRAC and ISSDC near Bengaluru. Equipped with magnetic torquers and two star trackers, AstroSat has target acquisition accuracy of ~30″. The five principal scientific payloads on-board AstroSat are: (i) an Ultra Violet Imaging Telescope (UVIT) configured as two independent telescopes – one for far-UV (FUV), and another for near-UV (NUV) and visible wavelengths, (ii) a Soft X-ray Telescope (SXT), (iii) three Large Area Xenon Proportional Counters (LAXPCs), (iv) a Cadmium–Zinc–Telluride Imager (CZTI), and (v) a Scanning Sky Monitor (SSM). Table 1 gives a summary of the basic characteristics of these payloads. Figure 1 shows a photograph of the satellite (just before launch) with all the payloads. A more detailed description of AstroSat is given in Singh *et al.*[1], and that of its principal instruments for astronomical observations in a special issue of *Journal of Astrophysics and Astronomy* and elsewhere[2–9]. Here, we present its scientific objectives and preliminary results of observations of various types of cosmic X-ray sources.

Scientific objectives and some results from individual telescopes

AstroSat provides an unprecedented wide X-ray band combined with UV and optical telescopes for simultaneous observations of variable high-energy phenomena from cosmic sources with the objective of exploring, identifying and quantifying contributions of different components (e.g. thermal, non-thermal, blackbody, synchrotron, inverse-Compton and spectral lines) in X-ray sources, and thus to understand their nature and astrophysical processes in them. The observations carried out in the past year, though mostly focused towards its calibration, are already leading to new spectral and temporal studies to establish the capabilities of individual instruments. For example, UV imaging of normal, starburst and dwarf

Figure 1. AstroSat in a clean room at Sriharikota.

*For correspondence. (e-mail: kulinderpal@gmail.com)

Table 1. Main characteristics of the telescopes and detectors of AstroSat

UVIT: Two telescopes – FUV and NUV + Vis	
Angular resolution	1.5″ (FUV, NUV); 2.2″ (Vis)
Field of view	28′ (dia.)
Effective area and energy resolution	Depend on the filtre used (13 filtres + gratings)
Time resolution	1.7 ms
Bandwidth	1300–5500 Å
LAXPC: Three units – LX10, LX20 and LX30 (non-imaging)	
Maximum effective area*	8000 sq. cm (3–20 keV for all three units)
Field of view	1° × 1°
Energy resolution	12% @ 22 keV
Time resolution	10 μs
Bandwidth	3–80 keV
CZTI	
Angular resolution	8′
Maximum effective area	~500 sq. cm @ 60 keV
Field of view	6° × 6°
Energy resolution	5% @100 keV
Time resolution	1 ms
Bandwidth	20–100 keV
SXT	
Angular resolution	2′ (FWHM); 10′ (HPD)
Maximum effective area	~ 90 sq. cm (1.5 keV)
Focal plane plate scale	4.0″/pixel (40 μm)
Field of view	40′ (dia.)
Energy resolution	140 eV @ 6 keV
Time resolution	2.37 s (PC); 0.278 s (FW)
Bandwidth	0.25–7.0 keV
SSM: Three units	
Angular resolution	12′ × 2.5°
Maximum effective area	53 sq. cm (5 keV)
Field of view	22° × 100° (central unit); 26.8° × 100° (edge units)
Energy resolution	25% @ 6 keV
Time resolution	1 ms
Bandwidth	2.5–10 keV

galaxies in the local and distant universe are addressing the evolution of stellar populations. UVIT imaging of the open cluster NGC 188 has led to the discovery[10] of a hot star (17,000 ± 500 K) likely to be a post-AGB/HB (asymptotic giant branch/horizontal branch) star and companion to a cool star (6,000 ± 150 K) known as a blue straggler star (BSS). Such star systems are rare and ideal for the study of their chemical composition and to constrain the theories of their formation. Other examples of UVIT results are multiple rings of star formation in NGC 7217, images of the Small Magellanic Cloud, time variability during a recent re-brightening of an Intermediate Polar, FO Aqr, etc.[11].

The capability of CZTI to measure the polarization signals above 100 keV (ref. 12) has provided hints of a polarization signal being measured for a gamma ray burst (GRB) of fluence less than 2×10^{-5} ergs cm^{-2}. Detection of brighter GRBs is expected to provide a much more significant polarization signal that will help to clearly distinguish between various models of GRB prompt emission mechanism[13]. The CZTI has sensitivity matching that of the Fermi GBM and therefore can detect possible hard X-ray emission associated with gravitational wave events. Observations with LAXPC caught the micro quasar GRS1915+105 (a stellar-mass black hole accreting from a normal star producing an accretion disk and occasionally producing bipolar jets perpendicular to the disk) in a rare χ mode revealing many new features in its energy-dependent power spectra, e.g. a strong low-frequency (2–8 Hz) quasi-periodic oscillation (QPO) and its harmonic along with broadband noise, and with the QPO frequency changing rapidly (in a few hours) with source intensity[14]. In another well-known accreting black-hole binary system, Cyg X-1 (also see below), the power spectrum obtained by LAXPC shows two broad Lorentzian functions centred at ~0.4 and ~3 Hz with the rms of the low-frequency component showing a decrease from ~15% at ~4 keV to ~10% at ~50 keV, while the time lag between the hard (20–40 keV) and soft (5–10 keV) bands increases with energy for both the low- and high-frequency components[15]. Such observations help us understand the dynamics of X-ray binaries with black-hole companions. Similarly, observations with SXT are providing variability on long timescales of minutes to

days in many active galactic nuclei (AGN)[16] and complementing the LAXPC spectral data with simultaneously obtained high-quality spectra. Here, we provide a glimpse of several high-quality spectra obtained over a wide X-ray band from many types of X-ray sources, and some new results from the UVIT imaging of parts of the Cygnus Loop – an old supernova remnant (SNR).

Preliminary results from multi-wavelength observations with AstroSat

Cyg X-1: a stellar black-hole binary

Cygnus X-1 is an X-ray binary in which a stellar black hole is believed to accrete matter from a massive stellar companion. The in-falling material is heated to very high temperatures producing copious amounts of X-rays and with the X-ray emission passing through soft state (spectrum dominated by soft X-rays) and hard state (spectrum dominated by hard X-rays) during outbursts. AstroSat has now observed this source simultaneously over a wide energy band (0.3–7 keV with SXT, 3.0–80.0 keV with LAXPC and 25.0–100 keV with CZTI) on several occasions. Figure 2 shows the wide-band X-ray spectrum observed with AstroSat on 18 July 2016. Analysis of the spectrum shows that the source was in a hard state on that occasion. The spectrum has been well fitted with a model comprising of thermal Comptonization component, the disk blackbody component and a moderate reflection component along with a common absorber. The use of wide X-ray band enables us to determine many parameters of this model, usually fixed when using narrower X-ray bands. For example, SXT has helped in determining the absorption column density to be 5.4×10^{21} cm^{-2} (mostly local to the source). The seed photons for thermal Comptonization are assumed to be from the accretion disk at assumed temperature of 3×10^4 K, with reflecting efficiency required to be 0.12. The photon index of the primary component is determined to be 1.72, and the electron temperature is found to have an upper limit of 75 keV. Figure 2 also shows the X-ray spectra as observed from the source simultaneously in three X-ray telescopes along with the residuals from the best-fit model. The data are shown as observed to highlight the difference in the effective areas of the instruments.

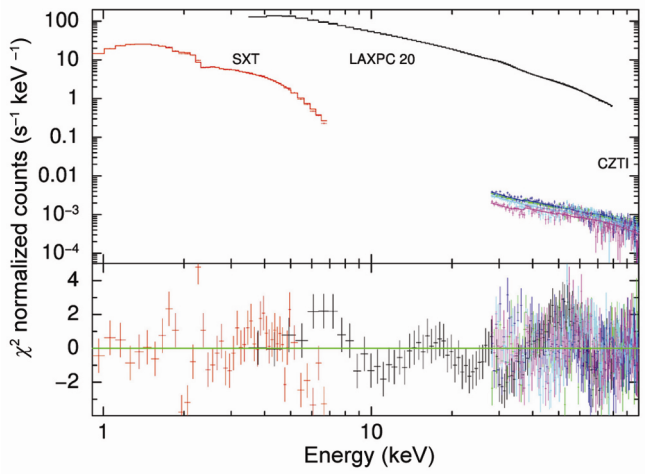

Figure 2. (Top panel) X-ray spectrum of a black-hole binary, Cyg X-1 as observed with SXT, LAXPC20 and CZTI along with the best-fit model shown as a histogram. The data do not overlap as the different instruments have different effective areas. (Bottom panel) Residuals from the best-fit model as contributions to χ^2. (Source: Cygnus X-1 date of Obs: 18 July 2016.)

NGC4151 Seyfert Galaxy: a supermassive black-hole in an active galaxy

AstroSat's multi-band capability is uniquely suited for probing the central engines of nearby AGN. Powered by accretion onto supermassive (10^7–10^9 suns) black-holes, AGN are the most luminous, continuously emitting and variable multiwavelength objects in the universe. Observations of AGN with AstroSat are already producing unique long looks in multi-colours and broadband X-ray spectra of Seyfert galaxies which are a type of radio-quiet AGN. AstroSat observed the nearby (62 million light years away) spiral galaxy NGC4151 hosting an intermediate Seyfert-type AGN for nearly 40 h in March 2017. This resulted in the net exposure time of 29.4 ks in SXT and 62.8 ks in LAXPC (the differences are due to the observation efficiencies being different). Figures 3–5 show the prelimiminary results from the analysis of SXT and LX10 data. The background-corrected SXT and LX10 light curves of NGC4151 in the common energy band of 3–8 keV (Figure 3), and the strong correlation and zero lag between them (Figure 4), clearly demonstrate the capability of AstroSat's simultaneous study in the soft and hard X-rays with the imaging SXT and non-imaging

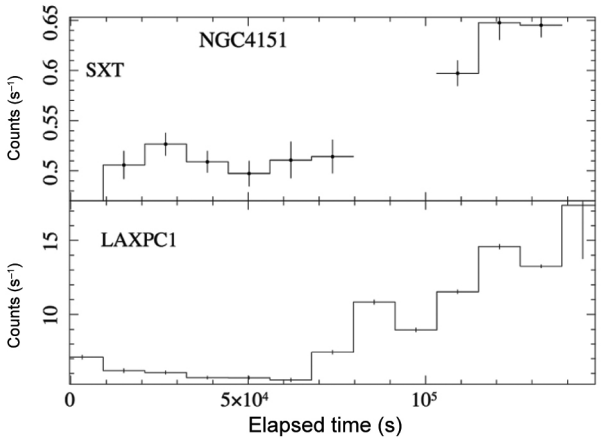

Figure 3. X-ray light curve seen with SXT (top) and LX10 (LAXPC1) (bottom) in the common energy band 3–8 keV.

LAXPC instruments. The wide X-ray band coverage (0.2–80 keV) with SXT/LAXPC is crucial to probe the different emission/absorption components arising from the close environments of Super Massive Black Holes (SMBHs). The spectral modelling of SXT and LX10 spectral data has resulted in the decomposition of direct or primary continuum which is absorbed at low energies, the scattered continuum and the reflected emission, including the iron emission line near 6.4 keV (Figure 5). The connection between the various spectral components and with the UV emission simultaneously observed with AstroSat/UVIT will play a crucial role in understanding the physics of central engines of AGN.

1ES1959+65: a blazar

Blazars (BL Lac) are a subclass of radio-loud AGN, seen through a relativistic jet emanating from an accreting SMBH, and are characterized by a dual-humped broadband spectral energy distribution (SED), high polarization, rapid flux variability and featureless optical spectrum. The low-energy part of SED (ranging from radio to soft-X rays) is usually explained by the electron synchrotron processes in the relativistic jet, whereas the high-energy emission (keV to TeV) is likely due to inverse Comptonization of lower-energy photons or proton synchrotron or through particle cascades (pion production and decay). Based on the SED, BLs are sub-classified as LBL (low-energy peaked BL Lac objects, if synchrotron peak $<10^{14}$ Hz), IBL (intermediate energy peaked BL Lac objects if the synchrotron peak is between 10^{14} and 10^{16} Hz), and HBLs (high-energy peaked BL Lac objects if the peak is $>10^{16}$ Hz). 1ES1959+650 (redshift = 0.048) is an HBL which has been showing episodes of flaring activities in TeV since October 2015 with corresponding activity at many other wavelengths.

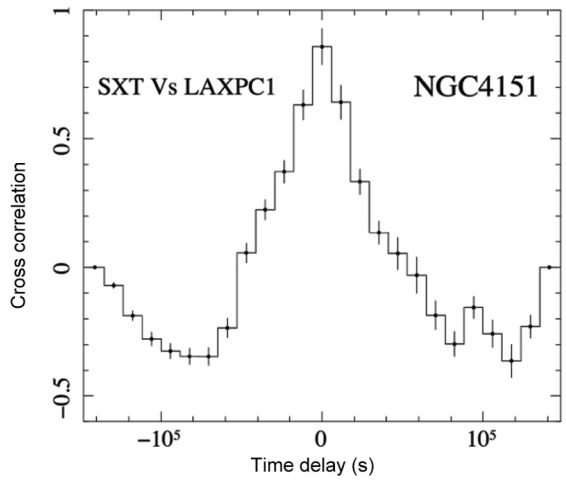

Figure 4. Cross-correlation of SXT and LAXPC 1 light curves shown in Figure 3 to establish the capability of SXT and LAXPC 1 combination to study time-lags.

A long observation of 1ES1959+65 with AstroSat was carried out during 3–6 November 2016; we have detected an X-ray flare during our observations (Figure 6). The rise to the peak and the fall to the quiescence are clearly visible. The complete X-ray flare is divided into four segments designated as T1, T2, T3 and T4, representing the different flux states of the flare. The broadband X-ray spectra from SXT + LAXPC were jointly fitted with a simple absorbed power law. The wide band provides an extremely accurate determination of the power-law index, and a detailed spectral analysis shows a subtle but clear hardening of spectra with intensity, the spectrum being hardest at the peak (T3) and regaining its initial softer state during the trailing part of the overall flare (T4).

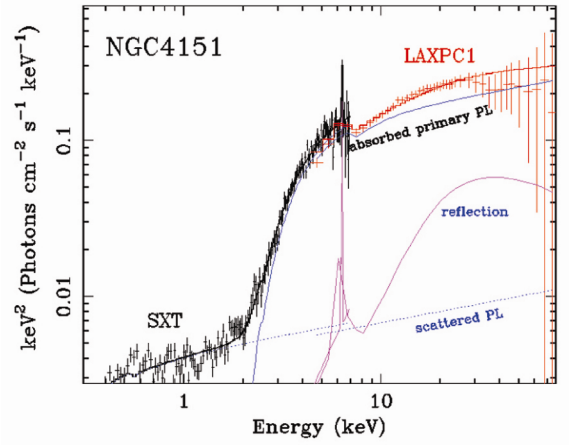

Figure 5. The unfolded (incident) spectrum of the Seyfert 1 Galaxy, NGC4151, based on the best-fit model fitted jointly to the SXT + LAXPC 1 spectra. The different model components are also shown.

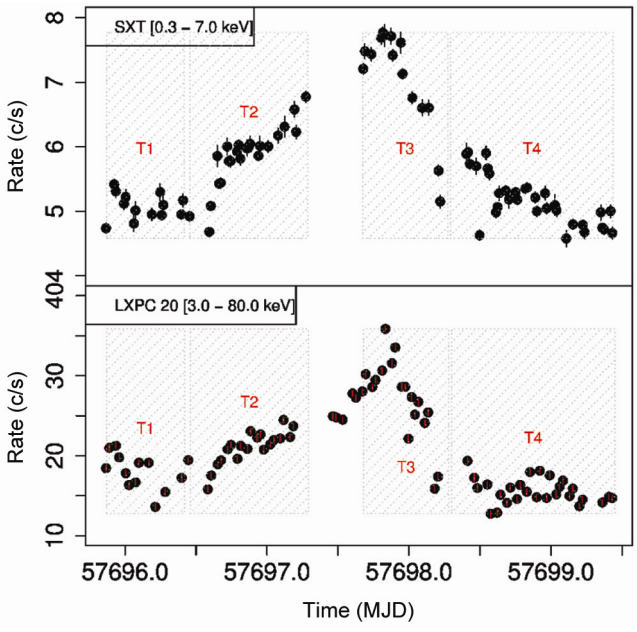

Figure 6. X-ray light curves of the blazar 1ES1959+65 showing the progression of a flare in two different energy bands observed in SXT (top) and LX20 (bottom).

These spectral changes are a clear indication of the evolution in the particle energy distribution during the onset of this X-ray flare.

Supernova remnants

SNRs are the result of spectacular explosions that massive stars undergo during the catastrophic end of their lives. These are the sites where charged particles are accelerated to very high energies – up to TeV. These explosions leave behind very compact objects like neutron stars or black holes like Cyg X-1 (above), besides enriching the interstellar material (ISM) with heavy nuclei formed through nucleosynthesis processes and ejected during the explosion. The shock produced by the explosion leads to non-thermal emissions near the shock front and thermal emissions from the enriched and heated plasmas from the remnant.

Further, since the progenitors of supernovae themselves are mostly unknown, SNRs serve as the only surviving diagnostic of the astrophysical nature of the progenitor star, its evolutionary path and its immediate environment. Given that X-ray and UV-bright galactic SNRs range in age from ~300 to 20,000 years, a multi-waveband study of these targets provides a unique opportunity to examine shock propagation and interaction in environments of varying densities. As the dense supernova (SN) ejecta plows into the ISM it creates varying morphologies, indicative both of the local properties of ISM as well as of the SN event itself. AstroSat's high UV spatial resolution, narrow-band UV-filters and high X-ray sensitivity spanning 0.3–100 keV, make it an ideal instrument to study the rapidly evolving properties of this plasma at different diagnostic temperatures – X-ray (10^6–10^7 K), FUV (10^4–10^5 K) and NUV (5000–8000 K).

The three examples below give a glimpse of the variety of results obtained from observing a young 1000-year-old SNR: Crab with dominant non-thermal emission and an energetic pulsar inside it, a younger (~350 years) SNR: Cassieopia A (Cas A) with highly ionized emission from the heated and ejecta-rich plasma, and a deep look at the Western Veil of an old and large remnant known as the Cygnus loop.

Crab Nebula and Pulsar: The Crab Nebula is the remnant of a historical supernova explosion recorded by Chinese astronomers in AD 1054. The core of the exploding star collapsed to form the Crab Pulsar, a neutron star spinning on its axis at 33.7 ms period. The nebula consists of expanding gaseous filaments that radiate primarily in the optical band, and an interior filled with relativistic electron–positron plasma generated by the pulsar[17]. These relativistic particles have a non-thermal energy distribution and generate a broadband power-law radiation spectrum covering radio to gamma rays. The pulsar too is a prolific emitter of non-thermal, power-law radiation over this entire electromagnetic range. Due to its bright and steady emission, Crab has long been considered a primary calibration standard in X-ray and gamma-ray astronomy. AstroSat has made several observations of the Crab since its launch in order to calibrate and characterize its X-ray payloads. Periodic observations of the Crab continue to be made in order to track changes in instrument calibration, if any. The Crab observations have served to cross-calibrate the spectral and timing characteristics of all the AstroSat instruments, and has also led to a clear detection of hard X-ray polarization by the CZTI payload (Vadawale *et al.*, in preparation). Figure 7 shows the pulse profile of the Crab Pulsar observed by AstroSat LAXPC and CZTI instruments. The gradual change in pulse shape as a function of energy as seen here matches that reported by earlier space missions.

Simultaneous observations of the Crab Pulsar with AstroSat and ground-based radio observatories have

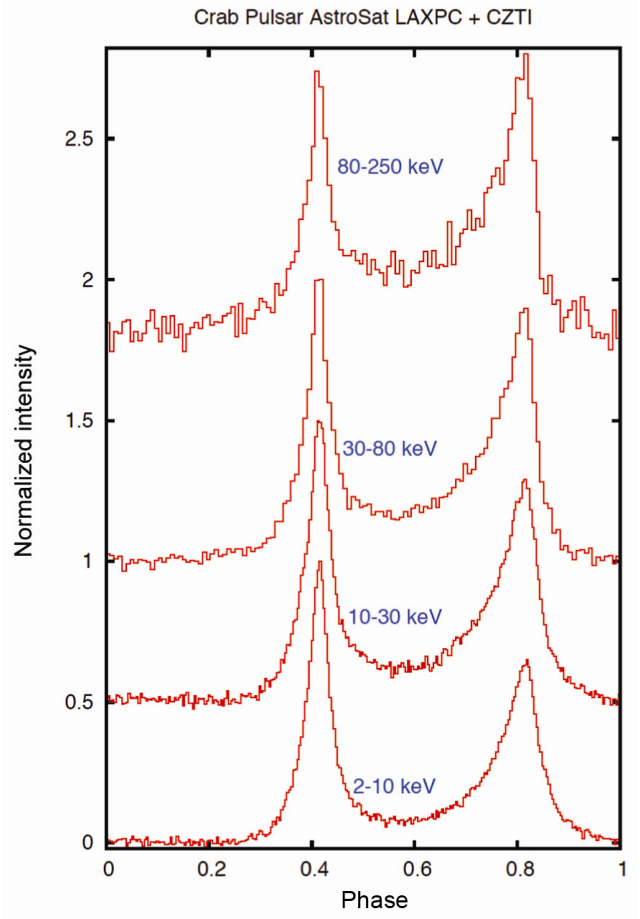

Figure 7. Pulse profile in different energy bands of the 33.7 ms pulsar in the Crab. The profiles are vertically shifted relative to each other to make them visible. The bottom two profiles are obtained from LAXPC data, and the top two from the simultaneous CZTI observation. The energy dependence of the relative intensity of the two pulse peaks is clearly seen and the known energy dependence of the pulse profile is well reproduced, demonstrating the capability of AstroSat.

demonstrated the stability and accuracy of the on-board timing of AstroSat. Emission from the Crab is derived from the rotational energy of the pulsar, causing it to spin down. Change in the spin period of the pulsar by less than 10 ns can be easily detected by AstroSat within a few hours[18].

Figure 8 shows the broadband X-ray spectrum of Crab observed on 31 March 2016 simultaneously with all the X-ray telescopes on-board AstroSat. Data from SXT (PC mode), LX20 and the four quadrants of CZTI were fitted jointly with the same model and the best-fit model is also shown in Figure 8, with the residuals in the lower panel showing the quality of the fit as a function of energy. Data from the central portion (radius < 2′) of SXT were excluded to avoid pile-up in the CCD. Data from all the instruments fit well with a power law having the photon index of 2.11 and low-energy absorption column of 3.5×10^{21} cm^{-2} of equivalent hydrogen atoms. The model parameters and energy flux are in good agreement with the previous measurements of Crab's spectrum with other X-ray observatories. Differences of relative normalizations seen within the instruments are being resolved using this measurement of the standard candle.

Cassiopeia A (Cas A)*:* This is the youngest (~350 years) SNR in our galaxy. Cas A is supposed to have evolved from a massive progenitor and its ejecta are thus enriched with heavy elements seen in its optical and X-ray emission. Its X-ray emission mostly arises from a highly clumped shell of reverse-shocked ejecta spread over a radius of ~2′ with a thickness of ~17″, with slightly weaker emission coming from a bigger shell of radius 2.5′, where the forward shock meets the interstellar medium[19]. A power law detected by the Beppo-SAX is thought to be coming from a non-thermal tail seen in the hard X-ray spectrum[20]. Figure 9 shows the AstroSat X-ray spectra from SXT and LAXPC. Several emission lines originating from the hot plasma, most likely to be in non-equilibrium due to its very young age are also marked in Figure 9. A power-law tail with a photon index of ~3.4 is also detected, which is slightly steeper than the index seen with the Beppo-SAX. The spectrum shown here, however, still needs to be fitted with more realistic models of non-equilibrium plasmas before we can be sure about the measurement of the power-law index.

The Witch's Broom in the Cygnus Loop: The images and spectra compiled in Figure 10 show the first AstroSat observations of a segment of the Cygnus loop – NGC 6960 – which comprises a part of the Western Veil (colloquially known as 'Witch's Broom', or the 'Finger of God'), observed simultaneously in FUV, NUV and soft X-rays (0.2–3.5 keV). Earlier, terrestrial observations of this loop in H-alpha[21] had revealed the presence of multiple shock fronts, caused by shock diffraction through dense clouds in this region. The AstroSat/UVIT NUV-N2 image of this region shown in Figure 10 reveals structures similar to the optical, and shows strong Mg abundance in the dense clouds. Similar shock morphology is also observed in the AstroSat UVIT-FUV image (which is a composite of images in the FUV–BaF2, FUV–Sapphire and FUV–Si bands), dominated by C IV (1550 A) and He II (1640 A; see Figure 10), suggesting significant enhancement of these elements in this region. Similar elemental abundances have been seen earlier in the International Ultra-violet Explorer (IUE) spectrum (also shown in Figure 10), taken over a much smaller 20″ × 2″ aperture. Since line strengths serve as tracers of both the ambient thermodynamic conditions as well as the abundances, the 3D characteristics of this region appear to have both hot and cool components, rich in Mg, He, C, Si and Fe. Similar abundance distributions are also seen in the X-ray spectrum of this region, obtained from SXT (Figure 10).

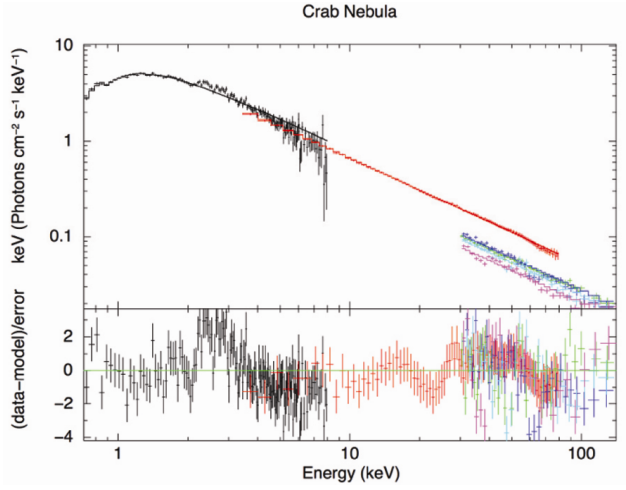

Figure 8. The incident photon X-ray spectrum of Crab Nebula observed with AstroSat: SXT (black) + LAXPC (red) + CZTI (blue, cyan, green, magenta for 4 units).

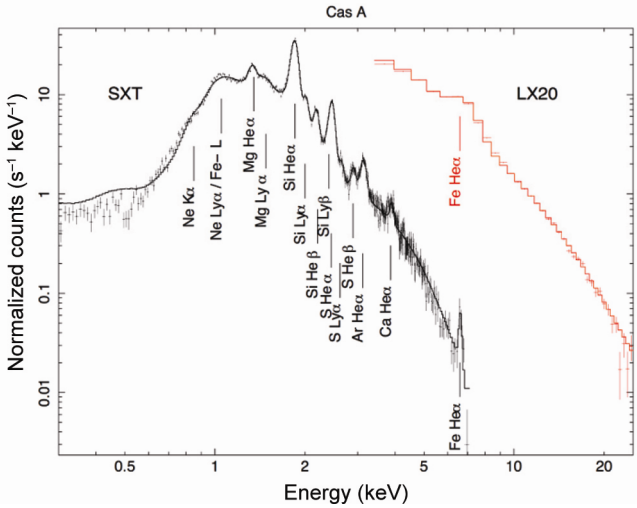

Figure 9. The Cas A spectrum observed with AstroSat: SXT and LX20.

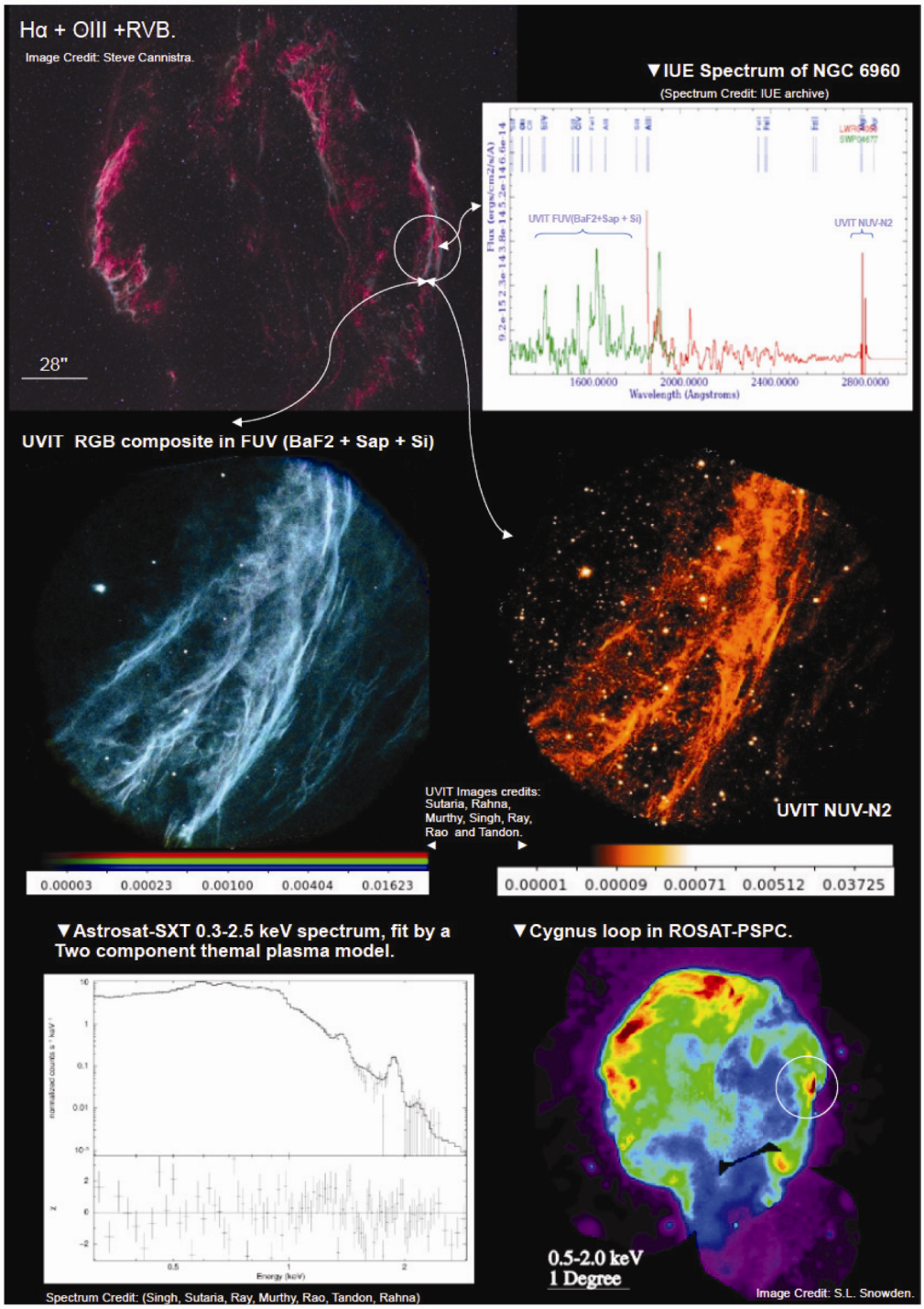

Figure 10. The Cygnus Loop and the Witch's Broom. An optical (top left) and X-ray (bottom right) image of the full nebula are shown, a circle in each marking the AstroSat field of view. The optical image is courtesy Steve Cannistra (www.starrywonders.com), reproduced here with permission. The ROSAT-PSPC X-ray image is obtained from the NASA HEASARC archive and is attributed to S. L. Snowden (Levenson *et al.*[22]). The middle row displays the AstroSat UVIT images in FUV and NUV bands. (Bottom left) SXT spectrum of the region and (top right) UV spectrum from the IUE archive.

1. Singh, K. P. *et al.*, ASTROSAT mission. In Proceedings of SPIE, Space Telescopes and Instrumentation 2014: UV to Gamma Ray (eds Takahashi, T., den Herder, J.-W. A. and Bautz, M.), 2014, vol. 9144, pp. 91441S-1 to S-15 Montreal; doi: 10.1117/12.2062667.
2. Bhalerao, V. *et al.*, The cadmium zinc telluride imager on AstroSat. *JApA*, 2017, **38**, 31–40.
3. Ramadevi, M. C. *et al.*, Early in-orbit performance of scanning sky monitor onboard AstroSat. *J. Astrophys. Astr,* 2017, **38**, 32–34.
4. Singh, K. P. *et al.*, In-orbit performance of SXT aboard AstroSat. In Proceedings of SPIE, Space Telescopes and Instrumentation 2016: Ultraviolet to Gamma Ray (eds den Herder, J.-W. A., Takahashi, T. and Bautz, M.), 2016, vol. 9905, pp. 99051E-1 to E-10; doi:10.1117/12.2235309.

5. Singh, K. P. *et al*., Soft X-ray focusing telescope aboard AstroSat: design, characteristics and performance. *J. Astrophys. Astr.*, 2017, **38**, 29.
6. Subramaniam, A. *et al.,* In-orbit performance of UVIT on ASTROSAT. In Proceedings of SPIE, Space Telescopes and Instrumentation 2016: Ultraviolet to Gamma Ray (eds den Herder, J.-W. A., Takahashi, T. and Bautz, M.), 2016, vol. 9905, pp. 99051F-1 to F-10; doi:10.1117/12.2235271 (arxiv: 1608.01073).
7. Tandon, S. N. *et al.*, In-orbit performance of UVIT and first results. *J. Astophys. Astr*., 2017, **38**, 28.
8. Vadawale, S. V. *et al*., In-orbit performance AstroSat CZTI. In Proceedings of SPIE, Space Telescopes and Instrumentation 2016: Ultraviolet to Gamma Ray (eds den Herder, J.-W. A., Takahashi, T. and Bautz, M.), 2016, vol. 9905, pp. 99051G-1 to G-11.
9. Yadav, J. S. *et al*., In Proceedings of SPIE Space Telescopes and Instrumentation 2016a: Ultraviolet to Gamma Ray (eds den Herder, J.-W. A., Takahashi, T. and Bautz, M.), 2016, vol. 9905, pp. 99051D; doi:10.1117/12.2231857.
10. Subramaniam, A. *et al*., A hot companion to a blue straggler in NGC 188 as revealed by the ultra-violet imaging telescope (UVIT) on AstroSat. *ApJL*, 2016, **833**, L27–L31.
11. Tandon, S. N., Ghosh, S. K., Hutchings, J., Stalin, S. and Subramaniam, A., Ultraviolet Imaging Telescope (UVIT) on AstroSat. *Curr. Sci.*, 2017, **113**(4), 583–586.
12. Chattopadhyay, T., Vadawale, S. V., Rao, A. R., Sreekumar, S. and Bhattacharya, D., Prospects of hard X-ray polarimetry with Astrosat-CZTI. *Experiment. Astr*., 2014, **37**, 555–577.
13. Rao, A. R. *et al*., AstroSat CZT imager observations of GRB 151006A: timing, spectroscopy, and polarization study. *ApJ*, 2016, **833**, 86–95.
14. Yadav, J. S. *et al*., AstroSat/LAXPC reveals the high-energy variability of GRS 1915+105 in the X class. *ApJ*, 2016, **833**, 27–35.
15. Misra, R. *et al*., AstroSat/LAXPC observation of Cygnus X-1 in the hard state. *ApJ*, 2017, **835**, 195–200.
16. Singh, K. P., Dewangan, G. C., Chandra, S., Bhattacharayya, S., Chitnis, V., Stewart, G. C. and Westergaard, N. J., Soft X-ray focusing telescope aboard AstroSat: early results. *Curr. Sci.*, 2017, **113**(4), 587–590.
17. Buhler, R. and Blandford, R., The surprising Crab pulsar and its nebula: a review. *Rep. Prog. Phys.*, 2014, **77**, 066901 (pp. 15).
18. Fabian, A. C., Willingale, R., Pye, J. P., Murray, S. S. and Fabianno, G., The X-ray structure and mass of the Cassiopeia A supernova remnant. *MNRAS*, 1980, **193**, 175–188.
19. Favata, F. *et al*., The broad-band X-ray spectrum of the CAS A supernova remnant as seen by the BeppoSAX observatory. *A&A*, 1997, **324**, L49–L52.
20. Fesen, R. A., Kwitter, K. B. and Downes, R. A., H-alpha images of the Cygnus Loop – a new look at shock-wave dynamics in an old supernova remnant. *AJ*, 1992, **104**, 719–724.
21. Levenson, N. A., Graham, J. R. and Snowden, S. L., The Cygnus loop: a soft-shelled supernova remnant. *ApJ*, 1999, **526**, 874–880.

ACKNOWLEDGEMENTS. We thank M. C. Aarthy, S. Chandra, V. Chitnis, G. C. Dewangan, R. Misra, Anjali Rao, F. Sutaria, Md. Shah Alam and Avishek Basu for analysing data and providing us with the figures and results presented here in advance of their publications. We acknowledge the dedication and devotion of the AstroSat teams that worked on the hardware and software for the different instruments in TIFR, IUCAA, IIA, PRL, RRI, ISAC, VSSC, SAC, ISTRAC and ISSDC, and made it a reality. We thank the teams at the University of Leicester led by G. C. Stewart, and at the Candian Space Agency led by J. Hutchings for their contributions to AstroSat. We thank the mission operations at ISRO and POCs for ensuring the safety of operations and providing data on a daily basis.

doi: 10.18520/cs/v113/i04/602-609